

# Digital Topography Models for Martian Surfaces

Tomasz Stepinski and Ricardo Vilalta

**Abstract**—We introduce a concept of the digital topography model, an extension to the familiar notion of the digital elevation model. The new model is a multi-layer grid that stores various topographical information. It is used for an unsupervised automated classification of topography features in a landscape. The classification assigns topographically meaningful labels to all pixels in the model. The results are displayed as a thematic map of topography. Resultant topographical features are characterized and compared using statistics of their constituent pixels. We demonstrate the usage of our method by classifying and characterizing topography of landscape in the Tisia Valles region on Mars. We discuss extensions and further application of our method.

**Index Terms**—Digital topography, unsupervised classification, automated extraction of features, landscape characterization, Mars.

## I. INTRODUCTION

Mars is in the center of the current solar system exploration effort. In particular, there are presently three orbiters, remotely collecting information about Martian surface from their orbits. These are, NASA Mars Global Surveyor (MGS) [1] and Mars Odyssey Orbiter [2], and ESA Mars Express [3]. The orbiters are designed to collect information about Mars as a whole. This global information can be used to infer the planet's past and the geological processes responsible for its present state. The orbiters gather data that can be divided into three broad categories: imagery data, topography data, and spectral data.

Imagery data has been the first to be collected (starting with Mariner and Viking probes) and it continues to be used as the primary source of information about the Martian surface. A standard mapping technique of photogeologic interpretation of images [4] has been developed to identify the topographic, stratigraphic and tectonic relationship of surface units and to produce geologic maps. However, only a small percentage of Martian surface have been studied in details because geologic mapping based on photogeologic interpretation of images is a manual and laborious procedure. The lack of tools for automating some tedious tasks, and thus for enabling analysis of the bulk of remotely collected Martian data, extends beyond imagery data and into the topography and spectral data.

We have recognized that the field of planetary geomorphology in general, and Martian geomorphology in particular, can substantially benefit from using autonomous or semi-autonomous tools that automate certain aspects of analysis and enable examination of large datasets. In this paper we concentrate on a methodology for automating an analysis of Martian topography data. The Martian topography data

was gathered by the Mars Orbiter Laser Altimeter (MOLA) instrument [5] aboard the MGS spacecraft. This data was subsequently used to construct [6] global topographic maps of Mars in the form of digital elevation models (DEMs). Our goal is to develop an unsupervised automated method for classification and characterization of Martian topographic features. Fast and objective characterization of Martian topography would alleviate the tedious task of photogeologic interpretation of topographical features from images and would significantly speed up production of geologic maps.

In this paper we introduce a concept of digital topography model (DTM), an organization of topographical information that enables automated classification and statistical analysis of topographical features on Mars. The DTM is a significant extension of the familiar notion of the DEM. Individual pixels in the DTM carry an array of local and regional topographical information that allows assigning pixels to specific topographic formations. Thus, in our method, an automated recognition of topographical features is achieved on the local level of its constituent pixels by means of clustering algorithm that groups pixels carrying similar information into clusters corresponding to topographic features. Because the classification is achieved on the pixel level, its results can be conveniently visualized by means of a thematic map of topography. In addition, pixel-level classification makes possible characterization and comparison of different topographical formations using statistical analysis. Our method is general and can be applied to any surface, including other planetary surfaces and terrestrial surfaces.

The objective of this paper is to describe the novel concept of the DTM and to demonstrate how it can be used for an unsupervised, automated classification and characterization of Martian landscapes. The concept of the DTM is laid down in Section II and our classification method is described in Section III. The results of applying our method to Tisa Valles, a test site on Mars, are presented in Section IV. A statistical comparison between selected topographic formations identified for Tisa Valles is given in Section V. Section VI contains summary and discussion.

## II. DIGITAL TOPOGRAPHY MODELS

A DEM,  $\mathcal{E}(x, y)$ , is a quantized planar rectangular space where each pixel (labeled by  $x$  and  $y$ ) is assigned an elevation value  $\mathcal{E}(x, y) = z(x, y)$ . In a DTM,  $\mathcal{T}(x, y)$ , each pixel is assigned a list of  $N$  values,  $\mathcal{T}(x, y) = \{\mathcal{T}_1(x, y), \dots, \mathcal{T}_l(x, y), \dots, \mathcal{T}_N(x, y)\}$ , that includes, but is not limited to, an elevation. The DTM, viewed as a data structure, is a 3-D array consisting of  $N$  layers with each layer holding a different topographic information organized in a 2-D grid.

Manuscript received January 20, 2002; revised November 18, 2002.

T. Stepinski is with the Lunar and Planetary Institute, 3600 Bay Area Blvd., Houston, TX 77058, USA (e-mail: tom@lpi.usra.edu)

R. Vilalta is with the Dept. of Computer Science, University of Houston, 4800 Calhoun Rd., Houston, TX 77204, USA (e-mail: vilalta@cs.uh.edu)

By construction, the DTM is somewhat analogous to the concept of a multispectral image, but it pertains to topographical rather than imagery data. Unlike a multispectral image (see, for example [7]), where every layer contains an intensity of light measured at a particular part of a spectrum, the layers in the DTM contain variables with different physical meanings. In principle, information for each layer in the DTM could be collected independently, but in practice the data for all layers are derived from an elevation field.

In this paper we construct the DTM with  $N = 6$  layers. The first layer of the DTM,  $\mathcal{T}_1(x, y)$ , contains an elevation field,  $z(x, y)$ . We artificially modify the original elevation field using the so-called “flooding” algorithm. It identifies all enclosed depressions (pits) in  $z(x, y)$  and raises their elevation to the level of the lowest pour point around their edge thus producing a flooded elevation field  $z_f(x, y) \geq z(x, y)$ . A field  $\delta(x, y) = z_f(x, y) - z(x, y)$  has non-zero values only for pixels located inside depressions. Large values of  $\delta$  flag pixels located deep inside depressions. In the context of Martian topography, pixels located inside craters can be identified using the values of  $\delta$ . The second layer of the DTM,  $\mathcal{T}_2(x, y)$ , holds the values of  $\delta(x, y)$ .

For a given pixel  $(x_0, y_0)$  we calculate the set of slopes between it and the eight of its nearest neighboring pixels using the original elevation field. The pixel’s slope,  $s(x_0, y_0)$ , is the largest slope in this set. Pixels at the boundaries of the DTM, where slope cannot be determined, are assigned the value of -1. The third layer of the DTM,  $\mathcal{T}_3(x, y)$ , holds the values of  $s(x, y)$ . A different field of slopes,  $s_f(x, y)$ , is associated with the flooded elevation field and it constitutes the fourth layer of the DTM,  $\mathcal{T}_4(x, y) = s_f(x, y)$ . We also store pixels’ slope directions, but this information is not assigned to any layer. In flat areas slope directions are assigned using an algorithm developed in [8].

A contributing area,  $a(x_0, y_0)$  is the total number of pixels “draining” through a given pixel  $(x_0, y_0)$ . The term draining is used here as a metaphor for connectivity between different pixels in a landscape. A pixel counts toward the contributing area of  $(x_0, y_0)$  if there is a chain of slope directions linking it to  $(x_0, y_0)$ . In landscapes that are indeed subjected to rainfall, a contributing area is tantamount to a drainage area. Small values of  $a$  flag pixels located on topographic peaks, ridges, and divides. Large values of  $a$  flag potential streams. The field of contributing areas calculated for the flooded elevation field is denoted by  $a_f(x, y)$ . The fifth and sixth layers of the DTM,  $\mathcal{T}_5(x, y)$  and  $\mathcal{T}_6(x, y)$ , hold values of  $a(x, y)$  and  $a_f(x, y)$ , respectively.

The values for  $\mathcal{T}_1$  are taken directly from a DEM. The values for the layers  $\mathcal{T}_2$  to  $\mathcal{T}_6$  are calculated using a software suite TARDEM [9]. Note that a value assigned to a pixel in layers  $\mathcal{T}_2$ ,  $\mathcal{T}_5$ , and  $\mathcal{T}_6$  depends on information gathered from a neighborhood (of varying size) of this pixel. This makes pixels “aware” of their topographic context.

### III. CLASSIFICATION OF PIXELS IN THE DTM

Each pixel  $(x_0, y_0)$  in the DTM holds a 6-D vector,  $\{\mathcal{T}_1(x_0, y_0), \dots, \mathcal{T}_6(x_0, y_0)\}$ , that we call a descriptor because it contains information capable of determining the



Fig. 1. Viking orbiter image of Tisia Valles region on Mars. The center the image is located at 46.13°E, 11.83°S. The terrain shown is approximately 215 km west to east and 192 km south to north.

topographical context of that pixel. Our task is to perform an unsupervised classification of all pixels in the DTM based on similarity of the values of their descriptors. Two pixels are similar if  $\mathcal{T}(x_1, y_1)$  and  $\mathcal{T}(x_2, y_2)$  are close in the sense of Euclidian metric. We apply a clustering algorithm over the DTM that produces as output a set of  $k$  classes,  $\mathcal{C}_k = \{c_1, c_2, \dots, c_k\}$ , where each class  $c_i$  contains a list of pixels that are similar to each other. The set of classes is mutually exclusive and exhaustive. Because similar pixels correspond to similar topographical context, such classification can be used to produce a thematic map of topography,  $\mathcal{M}(x, y)$ , a 2-D array of the same dimensions as the planar dimensions of  $\mathcal{T}$ . Each pixel in  $\mathcal{M}$  is assigned a label  $c_i$  of a class to which a corresponding pixel in  $\mathcal{T}$  belongs.

We cluster the DTM using probabilistic clustering algorithm that follows the Expectation Maximization (EM) technique [10]. It groups vectors into classes by modeling each class through a probability density function. Each vector in the dataset has a probability of class membership and is assigned to the class with highest posterior probability. The number of classes is calculated using cross-validation [11]. Because a non-trivial DTM contains a large amount of data, a direct clustering via the EM technique is computationally expensive. To alleviate this problem we have devised the following procedure. First, we sample the DTM to create a smaller, initial dataset of pixels. This initial dataset is clustered into  $\mathcal{C}_k$  using the EM technique. The number of classes is calculated using cross-validation procedure. The remaining pixels are classified into  $\mathcal{C}_k$  using a decision tree learning algorithm [12] constructed on the basis of the initial dataset.

### IV. APPLICATION TO TISIA VALLES REGION

To demonstrate a utility of the DTM for producing a thematic map of topography on Mars, we have chosen a specific

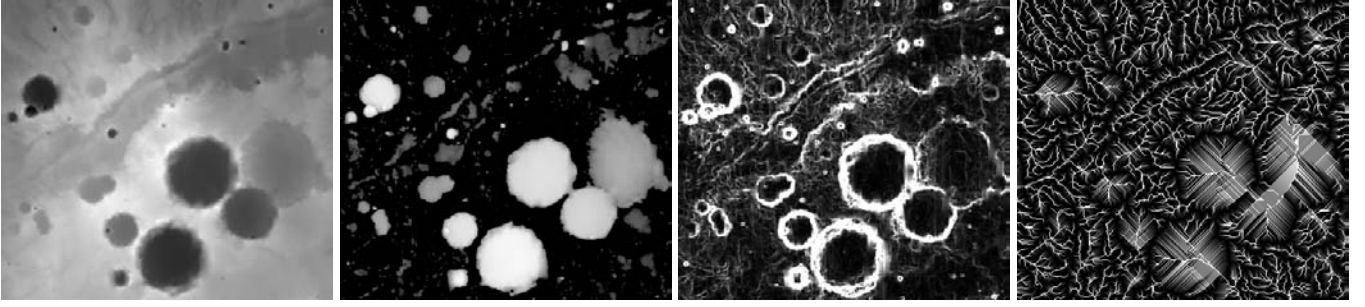


Fig. 2. Visual representation of topographical data layers constructed for Tisia Valles region on Mars. The layers are, from left to right, an elevation ( $\mathcal{T}_1$ ), the flooding adjustment ( $\mathcal{T}_2$ ), slopes ( $\mathcal{T}_3$ ), and the contributing area for flooded elevation field ( $\mathcal{T}_5$ ). The white to black gradient corresponds to the highest to the lowest values of variables.

region around Tisia Valles. Fig. 1. shows a Viking orbiter image of this region. The center of the image is located at  $46.13^\circ\text{E}$ ,  $11.83^\circ\text{S}$ . The terrain shown is approximately 215 km west to east and 192 km south to north. This is a typical ancient Martian surface, heavily cratered and showing presence of channels.

We have used digital elevation data from the MOLA Mission Experiment Gridded Data Record (MEGD) [6] to construct a DEM covering the terrain shown on Fig. 1. The DEM has a resolution of  $1/128$  degree, its dimensions are 385 rows and 424 columns. The DMT is constructed as described in Section II. The elevation range is from 1810 meters to 3580 meters. Flooding adjustment affects 31% of the pixels and the maximum flood is 947 meters. The largest value of  $a$  is 2005 pixels, slightly more than 1% of the total number of pixels. This indicates that an unadjusted elevation field lacks regional connectivity and breaks into a large number of small “basins.” However, the largest value of  $a_f$  is 68,625 pixels covering over 40% of the landscape area. Thus flooding adjusts the elevation field so it becomes regionally connected. Fig. 2. shows visual representation for four out of six layers of the DTM. It is clear from Fig. 2. that  $\mathcal{T}_2$  identifies craters,  $\mathcal{T}_3$  identifies sloped walls of craters, and  $\mathcal{T}_5$  identifies ridges and channels.

Because variables stored in different layers of the DTM have different physical meaning and different range of values we have normalized each variable so its values are in the range  $(0, 1)$ . This normalization assures that every variable contributes with equal weight to the “distance” between different pixels. The 40,000 pixels were randomly chosen from the normalized DTM to create an initial dataset. We have assured an uniform sampling to obtain an unbiased representation of all, even rare landscape features. Our clustering algorithm has classified these 40,000 pixels into 10 separable and exhaustive clusters. Remaining pixels were classified into those 10 clusters using a decision tree algorithm.

Fig. 3. is the thematic map of topography of the Tisia Valles region constructed on the basis on our classification. Pixel class membership is indicated by different shades of gray. Reviewing statistical properties of descriptors in each class we gave physical interpretations to these classes. The legend on Fig. 3. summarizes our interpretation. We have divided the 10 classes into 4 groups, craters (**C**), inter-crater plateau (**P**), ridges (**R**), and channels (**CH**).

The majority of pixels (73.7%) have been classified into the three classes grouped as **P**. The common features of these pixels are small values of  $\delta$ ,  $s$ , and  $a$ . The major discriminant between the three **P** classes is the value of an average elevation. The class **P1** (21% of pixels) is the high elevation plateau, the class **P2** (32%) is the medium elevation plateau, and the class **P3** (20.7%) is the low elevation plateau.

The second largest group of pixels (18.5%) have been classified into four classes grouped as **C**. The common features of these pixels are large values of  $\delta$  and  $s_f = 0$ . The major discriminant between the four **C** classes are the amount of flooding and the values of the slope. The class **C1** (2.8% of pixels) are pixels in deep craters. The class **C2** (7.8%) are pixels in medium-depth craters or pixels located up the walls of deep craters. The class **C3** (2.7%) are pixels located just below crater rims. The class **C4** (5.2%) are pixels located in shallow, partially buried craters.

The ridges (7.4%) consist of two classes grouped as **R**. The common features of these pixels are large values of  $s$ , very small values of  $a$ , and  $\delta = 0$ . The class **R1** (2.7%) are pixels located on the outside of crater rims. The class **R2** are pixels located at valley ridges, as well as on the outer walls of craters, below the pixels classified as **R1**. Finally, the class **CH** (0.4%) groups pixels characterized by large values of  $a$ . These pixels are the part of the landscape that constitutes the major drainage system. They could correspond to channels.

## V. STATISTICAL ANALYSIS

A thematic map exhibits information in a style that differs from more familiar presentations like, for example, a topographic map (a contour graph). Visually, a thematic map appears simpler and easier to interpret than a contour graph. This is because a process of assigning meaning to the raw data has been automated by the pixel classification scheme. A thematic map offers a pre-processed information. For example, on Fig. 3., class **C4** represents “shallow craters” regardless of the elevation of their location.

Notwithstanding the visual appeal of the resultant thematic map, the biggest advantage of the unsupervised classification scheme is its meaning-oriented annotation of all pixels in the DTM.

Automatically generated thematic map,  $\mathcal{M}(x, y)$  assigns meaning-carrying labels to the pixels. Adding  $\mathcal{M}(x, y)$  to the

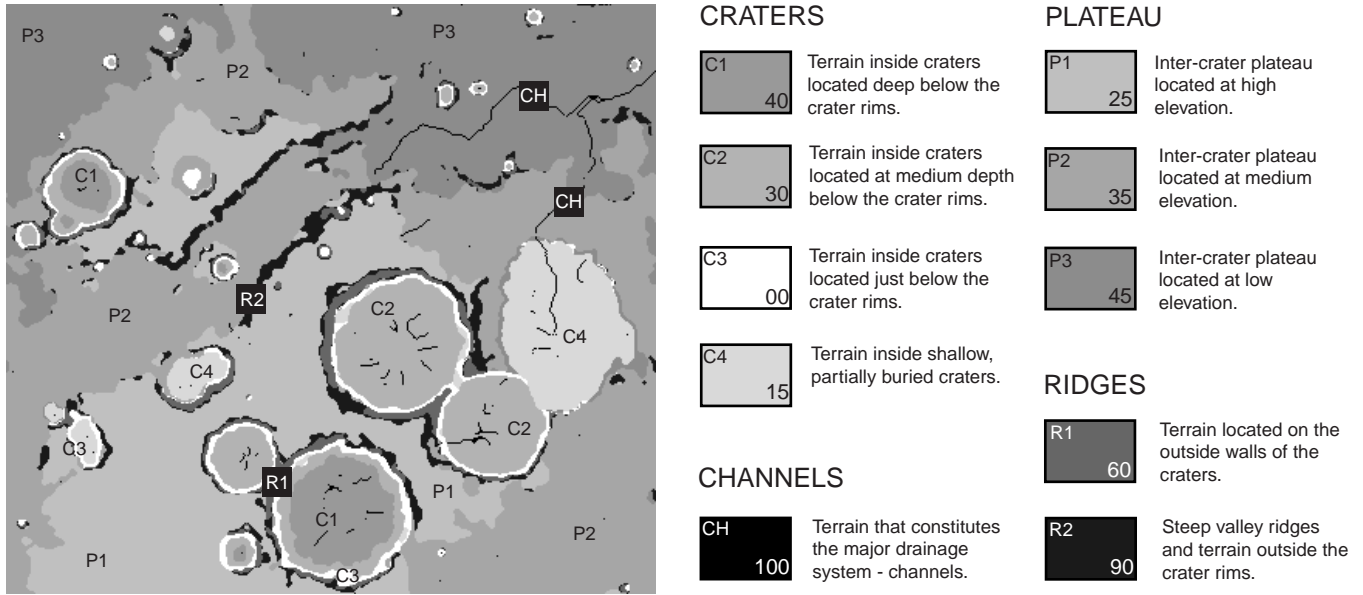


Fig. 3. Thematic map of topography for Tisia Valles region constructed from classification of pixels in the DTM. Pixels belonging to the same class are indicated by the same shade of gray. The legend on the right ascribes physical meaning to the classes. The symbol in the upper-left corner of a shade-coding rectangle is the class label. The number in the lower-right corner of the rectangle is the percentage of gray level.

$T(x, y)$  as an extra layer produces a data structure that is ideal for statistical analysis of landscapes. This additional layer serves as a filter or a mask to isolate particular features for characterization and/or comparison based on statistics of their constituent pixels.

To illustrate this point we have carried out a comparison of three plateau classes, **P1**, **P2**, and **P3** based on statistical analysis of properties of their constituent pixels. Specifically, we compare probability distribution functions (hereafter referred to as distributions and denoted by  $p$ ) of a given variable constructed for different classes. The distributions of elevations for the three plateau classes are not overlapping, thus an elevation is a variable that discriminates between them. However, the distributions of  $\delta$ ,  $s$ ,  $s_f$ , and  $a$  in the three plateau classes are almost identical. This confirms that all three classes pertain to the same type of terrain, an inter-crater plane, and differ only by an elevation.

Comparing classes **R1** and **C3** is interesting because they represent terrain near crater rims but outside and inside the crater, respectively. Comparing distributions of elevations reveals similar functional shapes of  $p_{R1}(z)$  and  $p_{C3}(z)$ . However  $p_{R1}(z)$  is shifted  $\sim 300$  meters towards the higher elevations. This shift is not unexpected because whereas the class **C3** consists exclusively of terrain inside the craters, the class **R1** consists of terrain outside the craters and the rims themselves. Perhaps more surprising is a similarity between  $p_{R1}(s)$  and  $p_{C3}(s)$ . Coinciding of the two local slope distributions suggests a symmetric elevation profile across a crater rim, whereas an asymmetric profile is more expected.

Finally, we compare the interiors of the two largest craters in the landscape depicted in Fig. 1. The first crater (referred to as crater A) is located in the lower portion of the scene and its interior is classified as **C1**. The second crater (referred

to as crater B) is located in the middle of the scene and its interior is classified as **C2**. Note, that in comparing interiors of these craters, we will use their locations, as well as  $\mathcal{M}(x, y)$  as masks for selecting pixels of interest. Distributions of elevation,  $p_A(z)$  and  $p_B(z)$  have similar shapes, however,  $p_B(z)$  is shifted  $\sim 100$  meters towards the higher elevations. That means that the floor of the crater B is at higher elevation than the floor of the crater A. Distributions of flooding adjustment,  $p_A(\delta)$  and  $p_B(\delta)$ , have similar shapes, but  $p_B(\delta)$  is shifted  $\sim 250$  meters towards the lower values of  $\delta$ . That means that the crater A is  $\sim 250$  deeper than the crater B. Its floor is located at the lower elevation not because the crater is located at lower terrain (in fact the crater A is located at the higher terrain), but because it is deeper. Comparing distributions of slopes,  $p_A(s)$  and  $p_B(s)$  shows that, in both cases, the distributions are skewed toward small slopes indicating relatively flat crater floors. However, the interior of crater B have relatively more pixels with higher slopes than the interior of crater A. This result may appear paradoxical given that the crater A is deeper. However, note that the interior of the crater A consist of class **C2** pixels in addition to the class **C1** pixels used in the comparison. The class **C2** pixels in crater A have relatively high slopes because they are located up the walls of the crater.

## VI. CONCLUSION AND DISCUSSION

In this paper we have introduced a concept of the digital topography model and have shown how it can be used for automated, unsupervised classification of topographical features in a landscape. It may appear surprising that a pixel-level classification, performed without any direct information about spatial relations yields highly integrated spatial structures (see Fig. 3.). The high spatial integrity of the resultant topographic

classes is crucial for the success of our method because topographical features are, after all, spatially coherent structures. The high spatial integrity of features identified by our method is attributed to the inclusion of  $\delta$ ,  $a$ , and  $a_f$  fields into the DTM. Although these variables are assigned at-a-pixel, they represent a regional information. In other words, they provide a connection between a local and a global scales. This is why our method, in its present form, is most useful for classification of landscapes having topographical basins (for example, craters). The presence of basins ensures a significant  $\delta$  field that, in turn, helps to enforce the spatial integrity of resultant structures. This is why planetary surfaces are the first to benefit from our method.

Further development of the DTM would make it more useful for terrestrial surfaces where topographical basins are relatively rare. Additional layers, holding scalar fields that, although assigned at-a-pixel, involve integrating information from a sliding window wrapped around a pixel, could be added to the DTM. Such variables, independent from  $\delta$  and  $a$ , would provide connection between local and regional scales and would assure spatial integrity of the resultant structures.

One such variable is regional surface roughness calculated from the elevation field. Regional roughness relates to a scatter of local elevations within a given region and can be quantified using the interquartile scale [13]. This quantity, denoted by  $r_q(x, y)$ , is a normalized distance between the first and the third quartile in a distribution of elevations collected from a square-shaped window wrapped around a pixel located at  $(x, y)$ . Because distributions of elevations are typically long-tailed,  $r_q$  is more robust estimator of roughness than, say, the standard deviation [14].

Similarly, we can define coherence,  $c(x, y)$ , of regional local slope directions. Because of discretization, there are only eight possible slope directions. We collect values of slope directions from all pixels in a square window centered at  $(x, y)$ . Next, the slope directions are re-labeled, the most abundant directions are labeled "1", the next most abundant directions are labeled "2" etc. We measure  $c(x, y)$  as a standard deviation of a distribution of re-labeled slope directions. A small value of  $c(x, y)$  indicates that slope directions within a neighborhood of  $(x, y)$  are preferentially aligned in the same direction. A large value of  $c(x, y)$  signals lack of any preference in slope direction within a neighborhood of  $(x, y)$ .

Both,  $r_q(x, y)$  and  $c(x, y)$  would be important additions to the DTM from the point of view of studying planetary surfaces, as well as studying terrestrial surfaces. In the terrestrial context yet more variables are conceivable. For example, following [15] we can include the field  $l(x, y)$  of hillslope-to-channel length. The length  $l(x, y)$  is the distance from a pixel at  $(x, y)$  to the nearest channeled pixel following the steepest descent path downslope. It is a scalar field that generalizes the traditional definition of globally defined drainage density. Finally, the concept of the DTM can be further extended to include layers of non-topographical information. For example, in geological context, an multispectral image carrying remotely collected mineralogical information can be appended to the DTM carrying topographical information. The classification of the combined digital topography/spectra model would group

pixels corresponding to specific topographic formations and having similar mineral composition. In the context of Mars, the Thermal Emission Imaging System (THEMIS) instrument aboard Mars Odyssey Orbiter takes multispectral images of Martian surface. The work is underway [16] to produce global mosaic of THEMIS images referenced to the MOLA mosaic. Once such mosaic is available, it would become practical to append Martian DTM with spectral information.

#### ACKNOWLEDGMENT

A portion of this research was conducted at the Lunar and Planetary Institute, which is operated by the USRA under contract CAN-NCC5-679 with NASA. This is LPI Contribution No. 12XX.

#### REFERENCES

- [1] A. L. Albee, F. D. Palluconi, and R. E. Arvidson, "Mars Global Surveyor Mission: Overview and Status", *Science*, vol. 279, pp. 1671-1672, 1998.
- [2] J. J. Plaut and the 2001 Mars Odyssey team, "Mars Odyssey Science: The First Year and Beyond", In *Lunar and Planetary Science XXXIV*, #1919, Lunar and Planetary Institute, Houston (CD-ROM), 2003.
- [3] A. F. Chicarro, "The Mars Express Mission - Initial Scientific Results from Orbit", In *Lunar and Planetary Science XXXIV*, #2174, Lunar and Planetary Institute, Houston (CD-ROM), 2004.
- [4] D. E. Wilhelms, "Geologic Mapping", In *Planetary Mapping*, (R. Greeley and R. Batson, Eds.), Cambridge, UK: Cambridge Univ. Press, pp. 209-260, 1990.
- [5] M. T. Zuber, D. E. Smith, S. C. Solomon, D. O. Muhleman, J. W. Head, J. B. Garvin, J. B. Abshire, and J. L. Bufton, "The Mars Observer Laser Altimeter Investigation", *J. Geophys. Res.*, vol. 97, no. E5, pp. 7781-7797, 1992.
- [6] D. Smith, G. Neumann, R.E. Arvidson, E.A. Guinness, and S. Slavney, "Mars Global Surveyor Laser Altimeter Mission Experiment Gridded Data Record", *NASA Planetary Data System*, MGS-M-MOLA-5-MEGDR-L3-V1.0, 2003.
- [7] D. Landgrebe, "The Evolution of Landsat Data Analysis", *Photogrammetric Ingeenering and Remote Sensing*, vol. LXIII, no. 7, pp. 859-867, 1997.
- [8] J. Garbrecht and L.W. Martz, "The Assigment of Drainage Direction Over Flat Surfaces in Raster Digital Elevation Models", *Journal of Hydrology*, vol 193, pp. 204-213, 1997.
- [9] D. G. Tarboton, R.L. Bras, and I. Rodriguez-Iturbe, "The analysis of river basins and channel networks using digital terrain data", *Technical Report* no. 326, Ralf M. Parsons Lab., MIT, Cambridge, 1989. (the software is available at [www.engineering.usu.edu/dtarb/](http://www.engineering.usu.edu/dtarb/)).
- [10] G. McLachlan and T. Krishnan, *The EM Algorithm and Extensions*. New York, NY: John Wilay and Sons, 1997.
- [11] P. Cheesman and J. Stutz, "Bayesian Classification (AutoClass) Theory and Practice", In *Advances in Knowledge Discovery and Data Mining*, (U. M. Fayyad, G. Piatetsky-Shapiro, P. Smyth and R. Uthurusamy, Eds.), MIT Press, pp. 153-180, 1996.
- [12] J. R. Quinlan, *C4.5: Program for Machine Learning*, San mateo, CA: Morgan Kaufmann, 1993.
- [13] G. A. Neumann and D. W. Forsyth, "High Resolution Statistical Estimation of Seafloor Morphology", *Marine Geophys. Res.*, vol. 17, pp. 221-250, 1995.
- [14] O. Aharonson, M. T. Zuber, and G. A. Neumann, "Mars: Northern hemisphere slopes and slope distributions", *Geophys. Res. Lett.*, vol. 25, pp. 4413-4416, 1998.
- [15] G. E. Tucker, F. Catani, A. Rinaldo, and R. L. Bras, "Statistical analysis of drainage density from digital terrain data", *Geomorphology*, vol. 36, pp. 187-202, 2001.
- [16] B. A. Archinal, L. Weller, S. Sides, G. Cushing, R. L. Kirk, A. Soderblom, and T. C. Duxbury, "Preparing for Themis Controlled Global Mars Mosaic", In *Lunar and Planetary Science XXXV*, #1903, Lunar and Planetary Institute, Houston (CD-ROM), 2004.